electronics

MDPI

Article

Modified Predictive Direct Torque Control ASIC with Multistage Hysteresis and Fuzzy Controller for a Three-Phase Induction Motor Drive

Guo-Ming Sung [1,2,*], Li-Fen Tung [1], Chong-Cheng Huang [1] and Hong-Yuan Huang [1]

[1] Department of Electrical Engineering, National Taipei University of Technology, Taipei 10608, Taiwan; savrina@stcomponent.com (L.-F.T.); vamprise123@gmail.com (C.-C.H.); hyhuang0118@gmail.com (H.-Y.H.)
[2] Research and Development Center for Smart Textile Technology, National Taipei University of Technology, Taipei 10608, Taiwan
* Correspondence: gmsung@ntut.edu.tw

Abstract: This paper proposes a modified predictive direct torque control (MPDTC) application-specific integrated circuit (ASIC) with multistage hysteresis and fuzzy controller to address the ripple problem of hysteresis controllers and to have a low power consumption chip. The proposed MPDTC ASIC calculates the stator's magnetic flux and torque by detecting three-phase currents, three-phase voltages, and the rotor speed. Moreover, it eliminates large ripples in the torque and flux by passing through the modified discrete multiple-voltage vector (MDMVV), and four voltage vectors were obtained on the basis of the calculated flux and torque in a cycle. In addition, the speed error was converted into a torque command by using the fuzzy PID controller, and rounding-off calculation was employed to decrease the calculation error of the composite flux. The proposed MDMVV switching table provides 294 combined voltage vectors to the following inverter. The proposed MPDTC scheme generates four voltage vectors in a cycle that can quickly achieve DTC function. The Verilog hardware description language (HDL) was used to implement the hardware architecture, and an ASIC was fabricated with a TSMC 0.18 μm 1P6M CMOS process by using a cell-based design method. Measurement results revealed that the proposed MPDTC ASIC performed with operating frequency, sampling rate, and dead time of 10 MHz, 100 kS/s, and 100 ns, respectively, at a supply voltage of 1.8 V. The power consumption and chip area of the circuit were 2.457 mW and 1.193 mm × 1.190 mm, respectively. The proposed MPDTC ASIC occupied a smaller chip area and exhibited a lower power consumption than the conventional DTC system did in the adopted FPGA development board. The robustness and convenience of the proposed MPDTC ASIC are especially advantageous.

Keywords: induction motor; predictive direct torque control (PDTC); fuzzy PID controller; multistage hysteresis controller; discrete multiple-voltage vector (DMVV); rounding-off calculation; Verilog hardware description language (HDL); application-specific integrated circuit (ASIC)

Citation: Sung, G.-M.; Tung, L.-F.; Huang, C.-C.; Huang, H.-Y. Modified Predictive Direct Torque Control ASIC with Multistage Hysteresis and Fuzzy Controller for a Three-Phase Induction Motor Drive. *Electronics* **2022**, *11*, 1802. https://doi.org/10.3390/electronics11111802

Academic Editor: Esteban Tlelo-Cuautle

Received: 26 April 2022
Accepted: 3 June 2022
Published: 6 June 2022

1. Introduction

The use of direct torque controllers in three-phase induction motor (IM) drives is common because of the fast torque and flux control of these controllers [1,2]. Nevertheless, the traditional hysteresis controller is the most frequently used controller in such drives. Conventional direct torque control (DTC) is a simple and robust method that is associated with the disadvantages of high torque, flux ripples, and switching losses [3]. After considerable research effort, the performance of the conventional DTC method was improved. In DTC space vector modulation (SVM), torque ripples and switching losses are reduced using a predictive controller, which increases the complexity of DTC [4]. DTC SVM with an imaginary switching time requires low memory and does not require sector determination;

thus, this method retains the simplicity of conventional DTC and produces the same results as DTC SVM with predictive controllers [5].

Compared with conventional proportional–integral–derivative (PID) controllers, the fuzzy PID controller exhibits a more favorable dynamic response and static deviation in a DTC system [6]. In [7], a novel predictive DTC (PDTC) scheme was proposed that maintains the motor torque, stator flux, and inverter's neutral-point potential within the set hysteresis bounds and minimizes the switching frequency of the inverter to reduce the torque and flux ripples. The complexity of the aforementioned PDTC model results from the computation of the stator flux reference and the prediction of the stator flux in the next cycle. The inverter switching frequency of the aforementioned scheme is on average 16.5% lower than that of a traditional DTC scheme [8]. Computational control solutions are becoming computationally and economically feasible, with versatile and flexible control algorithms being developed for electric motor drives. In comparison with a traditional PID regulator, a fuzzy PID regulator is more effective in improving the speed response and stability of a DTC system. In [9], an alternative control strategy that involved using a permanent-magnet synchronous-motor (PMSM) drive was proposed on the basis of the model system, prediction components, and optimization problem [10,11]. This strategy can improve speed tracking and strengthen robustness against disturbance and uncertainties when the suggested DTC controller is employed.

In [12], a DTC scheme was presented for a matrix-converter-fed IM drive system. A matrix converter is a single-stage AC–AC power conversion device without DC-link energy storage elements. Because of the properties of matrix converters, the pseudo DC-link provides three voltages, namely, high, middle, and low voltages. Three states are observed at each space vector location according to the SVM generated using a matrix converter. By selecting a suitable switching table, the electromagnetic torque ripple of the IM was effectively reduced, and a satisfactory servo drive was achieved. Moreover, no complicated computation was involved in the aforementioned scheme, and the matrix converter constituted a precise servo-drive control system. Next, the hysteresis band (HB) controller was used to enhance dynamic performance. Although the HB controller is extensively used in voltage source inverters and inverter-based drive systems, it is rarely used in matrix converters or matrix-converter-based motor drives [13]. The sinusoidal-band hysteresis controller generated low harmonic content at a high average switching frequency. The aforementioned scheme is simple and has a low computation burden. This scheme can be applied to IMs and other machines, such as PMSMs. A design method was presented for variable structure system control in [14] based on a differential geometric approach, and it was intended to deal with the class of nonlinear systems in the control with uncertainties and disturbances. The main goals of this method are robustness, tuning simplicity, chattering reduction, and reaching mode control. A robust controller was designed for the wind subsystem of an electricity generating hybrid systems (EGHS) [14]. A wind power system under failures was presented in the lubricant system, and a procedure was provided to detect the failure. A model-based fault detection filter was designed to detect DC/DC converter failure in a wind system [15].

A tariff plan is recommended for completely eliminating round-off error and reducing the operations on floating-point numbers [16,17]. Two round-off error models are used in fixed-point arithmetic: a generic model with no assumptions on the predicted system or weight matrices and a parametric model that exploits the Toeplitz structure of the linear model predictive control (MPC) problem for a Schur stable system. The experimental results of these models indicate that the resource usage, computational energy, and execution time vary significantly with the adopted field-programmable gate array (FPGA) [18,19]. Next, the feasibility condition for the design parameters was verified, and the optimized design parameters were rounded off to the nearest feasible design values [20]. Lastly, an application-specific integrated circuit (ASIC) was used to enable the direct control of the stator flux and instantaneous torque without a complex algorithm [21]. A modified DTC ASIC with five-stage fuzzy hysteresis and a fuzzy PID speed controller was used to reduce

the torque and flux ripples induced by the limited vector voltages and low speed response in a traditional DTC [22]. A modified DTC ASIC not only improves the stability of the motor control system, but also reduces power consumption.

In this paper, we propose a modified PDTC (MPDTC) ASIC with fuzzy seven-stage hysteresis and a fuzzy PID controller. Fuzzy controllers and round-off calculations can significantly improve the performance of three-phase IM drive systems. The remainder of this paper is organized as follows. Section 2 describes the circuit design of the proposed MPDTC ASIC for an IM drive system, and Section 3 presents the simulation and experimental results for functional verification. Lastly, Section 4 presents the conclusions of this study.

2. Circuit Design of the Proposed MPDTC ASIC

Figure 1 depicts the block diagram of the proposed MPDTC ASIC with fuzzy seven-stage hysteresis and a fuzzy PID controller for a three-phase IM drive system. This ASIC contains a three- to two-phase transformation block, voltage calculation block, flux calculation block, torque calculation block, sector selection block, speed feedback block, predictive calculation block, fuzzy PID controller, torque error fuzzy controller, flux error fuzzy controller, five-stage hysteresis controller, seven-stage hysteresis controller, modified discrete multiple-voltage vector (MDMVV) switching table, and short-circuit prevention block. All the functional blocks were designed using the Verilog hardware description language (HDL) and verified using an FPGA development board. Lastly, the proposed ASIC was fabricated with a TSMC 0.18 µm 1P6M CMOS process to reduce power consumption, and enhance the robustness and convenience of the three-phase IM drive. All symbols used in Figure 1 are shown in Appendix A to enhance the reading.

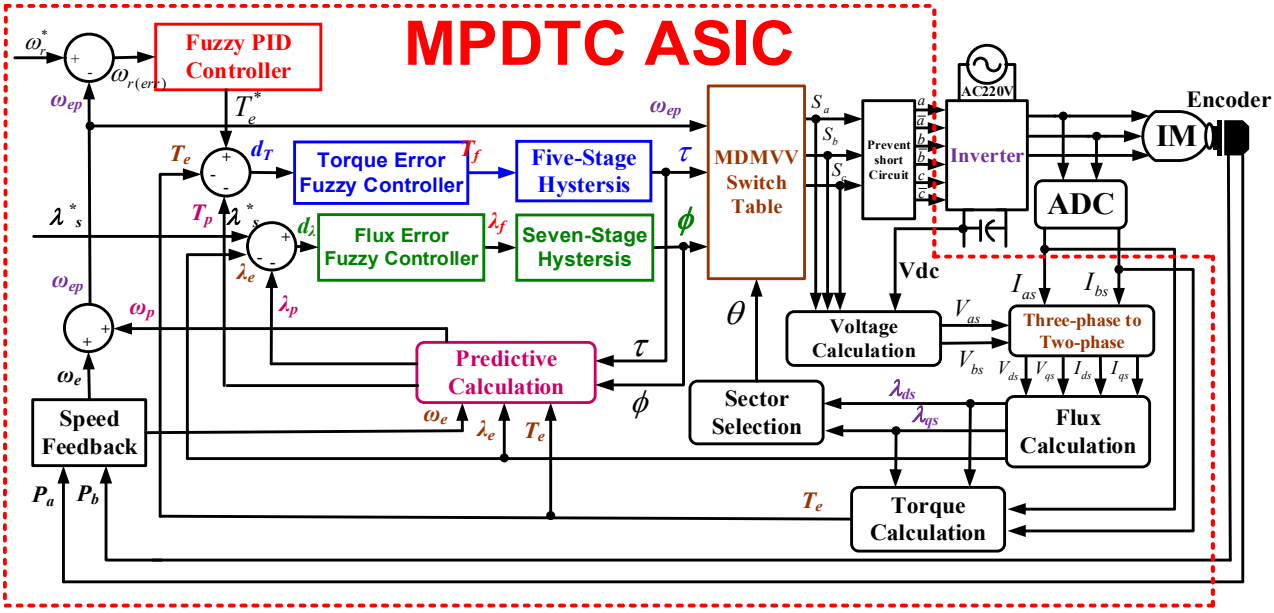

Figure 1. Block diagram of the proposed MPDTC ASIC with fuzzy seven-stage hysteresis and a fuzzy PID controller for s a three-phase IM drive system.

2.1. Coordinate Transformation and Calculation Formulas

Coordinate transformation from three phases (ABC axes) to two phases (DQ axes) was performed to reduce the calculation burden and increase the speed response. This transformation can be completed using the following trigonometric function [23]:

$$\begin{bmatrix} v_{ds}^{s} \\ v_{qs}^{s} \end{bmatrix} = \begin{bmatrix} 1 & 0 \\ 1/\sqrt{3} & 2/\sqrt{3} \end{bmatrix} \begin{bmatrix} v_{as}^{s} \\ v_{bs}^{s} \end{bmatrix} \quad (1)$$

$$\begin{bmatrix} i^s_{ds} \\ i^s_{qs} \end{bmatrix} = \begin{bmatrix} 1 & 0 \\ 1/\sqrt{3} & 2/\sqrt{3} \end{bmatrix} \begin{bmatrix} i^s_{as} \\ i^s_{bs} \end{bmatrix} \tag{2}$$

where $v^s{}_{as}$ (= V_{as}) and $v^s{}_{bs}$ (= V_{bs}) are three-phase voltages, $i^s{}_{as}$ (= I_{as}) and $i^s{}_{bs}$ (= I_{bs}) are three-phase currents, $v^s{}_{ds}$ (= V_{ds}) and $v^s{}_{qs}$ (= V_{qs}) are two-phase voltages, and $i^s{}_{ds}$ (= I_{ds}) and $i^s{}_{qs}$ (= I_{qs}) are two-phase currents.

Next, two-phase voltages V_{ds} and V_{qs} can be calculated using the three up-arm voltages of the U-, V-, and W-phases (S_a, S_b, and S_c, respectively). DC voltage V_{dc} is measured at the output terminal of the inverter as follows:

$$V_{ds} = \frac{V_{dc}}{3}(2S_a - S_b - S_c) \tag{3}$$

$$V_{qs} = \frac{\sqrt{3}}{3}V_{dc}(S_b - S_c) \tag{4}$$

The flux (φ) can be expressed in terms of the single-phase stator winding resistance R_s as follows:

$$\begin{bmatrix} \varphi^s_{ds} \\ \varphi^s_{qs} \end{bmatrix} = \frac{1}{p}\left\{ \begin{bmatrix} v^s_{ds} \\ v^s_{qs} \end{bmatrix} - R_s \begin{bmatrix} i^s_{ds} \\ i^s_{qs} \end{bmatrix} \right\},\ p = \frac{d}{dt} \tag{5}$$

According to the Laplace transform, variable p is defined as complex s, and T is the sampling period. The two fluxes $\varphi^s{}_{ds}$ and $\varphi^s{}_{qs}$ can then be expressed as follows [23]:

$$\begin{cases} \varphi^s_{ds}(z) = \frac{1}{z}\varphi^s_{ds}(z) + T \times \left[V^s_{ds}(z) - R_s \times i^s_{ds}(z)\right] \\ \varphi^s_{qs}(z) = \frac{1}{z}\varphi^s_{qs}(z) + T \times \left[V^s_{qs}(z) - R_s \times i^s_{qs}(z)\right] \end{cases} \tag{6}$$

The torque (T_e) is calculated on the basis of DTC theory by using (7), in which P is the number of motor poles.

$$T_e = \frac{3}{2}\frac{P}{2}\left(\varphi^s_{ds} i^s_{qs} - \varphi^s_{qs} i^s_{ds}\right) \tag{7}$$

when two magnetic fluxes λ_{ds} and λ_{qs} are obtained, the synthetic flux λ_{dqs} can be calculated using a square root circuit, round-off calculation circuit, and D-type flip-flop (DFF) circuit.

$$\lambda^s_{dqs} = \sqrt{\lambda^2_{ds} + \lambda^2_{qs}} \tag{8}$$

The square root is obtained using the shadow tree algorithm [1], and the DFF circuit is employed to complete synchronization using the clock signal (clk). The round-off calculation is used to reduce the calculation error of the square rooting circuit. Figure 2 illustrates the calculation blocks of the synthetic flux λ_{dqs}, namely, the square root, round-off calculation, and DFF circuits.

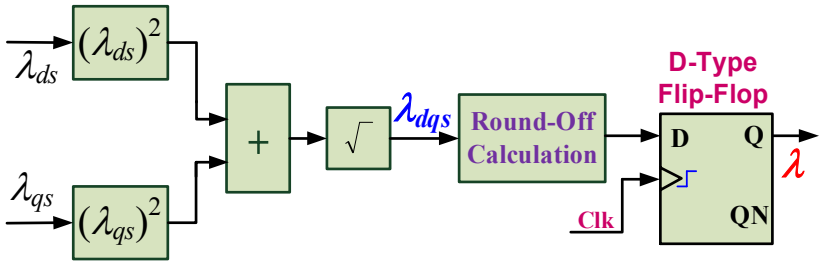

Figure 2. Calculation blocks of the synthetic flux with square root, round-off calculation, and DFF circuits.

To complete the round-off calculation, a calibration constant (*Cal*) is used to modify the output code of the rounding-down calculation (*RD*) with the input code *IN*. If *Cal* is less than or equal to 0, the output digital code (*RO*) does not change and is equal to *RD*. If

the *Cal* is greater than 0, the output digital code (*RO*) is equal to the rounding-down code (*RD*) + 1. *Cal* can be defined as follows:

$$\begin{aligned} Cal &= \left[IN - RD^2\right] - \left[(RD+1)^2 - IN\right] \\ &= 2 \times \left[IN - RD \times (RD+1)\right] - 1 \end{aligned} \tag{9}$$

The decision formula can be expressed as follows:

$$\begin{cases} RO = RD, & if\ Cal \leq 0 \\ RO = RD + 1, & if\ Cal > 0 \end{cases} \tag{10}$$

2.2. Sector Selection

The sector can be selected through the calculation of the two-phase magnetic fluxes λ_{ds} and λ_{qs} and synthesis magnetic flux λ_{dqs}. In general, the voltage space vector can be divided into six sectors, with each sector covering an angle of 60°. To simplify the analysis, the first quadrant of the coordinate plane is examined. If λ_{ds} and λ_{qs} are positive, the first quadrant includes the sectors S_1 and S_2, which extend from 0° to 30° and from 30° to 90°, respectively. In trigonometry, a relational equation can be expressed as follows:

$$\sqrt{3}\left|\lambda_{qs}\right| - \left|\lambda_{ds}\right| = 0 \tag{11}$$

If magnetic fluxes λ_{ds} and λ_{qs} are positive, the result of (11) is negative (<0) for sector S_1 and positive (>0) for sector S_2. Table 1 summarizes the sector selection for the proposed MPDTC ASIC. The output sector can be easily selected using this table [21].

Table 1. Sector selection of the proposed MPDTC ASIC.

$\sqrt{3}\,\lvert\lambda_{qs}\rvert - \lvert\lambda_{ds}\rvert$	λ_{ds}	λ_{qs}	Output Sector
<0	>0	>0	S1
<0	>0	<0	S1
<0	<0	>0	S4
<0	<0	<0	S4
>0	>0	>0	S2
>0	>0	<0	S6
>0	<0	>0	S3
>0	<0	<0	S5

2.3. Predictive Calculation Circuit

An MPC system is used to provide decoupled flux and torque control, and to reduce the torque and flux ripples in a three-phase IM drive system. The advantages of an MPC system include its retention of the benefits of the conventional DTC architecture and its light calculation burden in rapidly computing the motor's position [24]. Figure 3 presents the block diagram of an MPC system for stator flux error (λ_e), torque error (T_e), and speed error (ω_e) calculations. The proposed MPC DTC architecture can improve the control performance of an IM drive with high speed and high-precision motor control. As depicted in Figure 3, the delay (z^{-1}) block is implemented with a DFF circuit, and the subtraction block ($-$) is used to obtain the deviation between the present data D[k] and previous data D[k − 1]. The input code D[k] comprises the flux (λ_e), torque (T_e), and speed error (ω_e). Moreover, the absolute block (Abs.) provides the magnitude of the deviation. The multiplexer determines the output codes out[k], including λ_p, T_p, and ω_p, according to the control signals C[k] (τ or φ), from the hysteresis controllers.

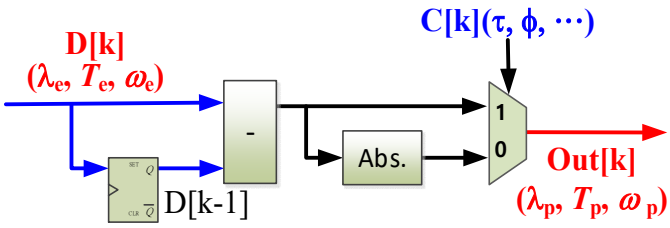

Figure 3. Block diagram of the predictive control model with input flux error (λ_e), torque error (T_e), and speed error (ω_e).

2.4. Fuzzy PID Controller

PID controllers are widely used for solving complex control problems, including the speed control problem of an IM drive. The traditional PID controller, which has a simple structure, low cost, and easy repairability, decides the values of K_p, K_i, and K_d by using the Ziegler–Nichols tuning method [25]. The general formula of a PID controller can be expressed as follows:

$$\frac{U(s)}{E(s)} = K_p + \frac{K_i}{s} + sK_d, \tag{12}$$

where s is a complex frequency. Parameters K_P, K_i, and K_d represent the proportional, integral, and derivative coefficients, respectively, which markedly influence the stability of the PID controller. A fuzzy PID controller can obtain optimal parameters more easily and efficiently than a nonfuzzy linear PID controller can.

Figure 4 presents a block diagram of the adopted fuzzy PID controller, which operates with an input error $e(t)$ (expressed as $e(t) = \omega^*_r - \omega_r$) and an input error variation $\Delta e(t)$. The fuzzy controller destination is determined by computing the parameters K_p and K_d by using the membership function and fuzzy rules. Integral coefficient K_i can be calculated using a constant α as follows:

$$K_i = \frac{K_p^2}{\alpha \times K_d} \tag{13}$$

The operating principle of the PID controller is to determine the output $u(t)$ with three coefficients, which can be calculated as follows:

$$u(t) = K_p e(t) + K_i \int_o^t e(\tau)d\tau + K_d \frac{de(t)}{dt} \tag{14}$$

After $u(t)$ is calculated, a closed-loop control procedure is executed for the IM drive. The self-adjusting mechanism is completed using the speed feedback ω_r. The fuzzy PID controller operates with adequate adaptability. The fuzzy rules of K_P, K_d, and α are listed in Tables 2–4, respectively [23]. Constant α is restricted to 4-level architecture, which is numbered from 2 to 5, and a minimal constant of 2 was set for PB and NB of input error variation $\Delta e(t)$. By setting the small constant α of 2, the operational range was restricted to 3 levels, PS, ZE, and NS, at input error variation $\Delta e(t)$. Input error $e(t)$ was also proportional to constant α. The large error $e(t)$ corresponded a large constant α at the PB or NB of input error $e(t)$. Table 4 can not only speed up the calculation, but also shorten the convergence time.

Table 2. Fuzzy rules of K_P.

e \ Δe	**PB**	**PS**	**ZE**	**NS**	**NB**
PB	PB	PB	PB	PB	PB
PS	PS	PB	PB	PB	PS
ZE	PS	PS	PB	PS	PS
NS	PS	PB	PB	PB	PS
NB	PB	PB	PB	PB	PB

Table 3. Fuzzy rules of K_d.

e \ Δe	PB	PS	ZE	NS	NB
PB	PS	PS	PS	PS	PS
PS	PB	PB	PS	PB	PB
ZE	PB	PB	PB	PB	PB
NS	PB	PB	PS	PB	PB
NB	PS	PS	PS	PS	PS

Table 4. Fuzzy rules of α.

Δe \ e	PB	PS	ZE	NS	NB
PB	2	2	2	2	2
PS	4	3	2	3	4
ZE	5	4	3	4	5
NS	4	3	2	3	4
NB	2	2	2	2	2

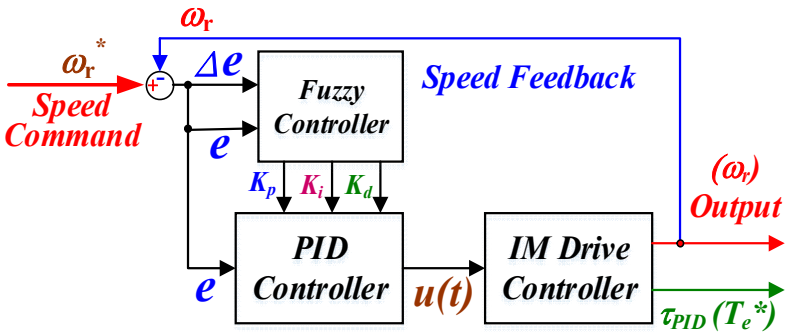

Figure 4. Block diagram of a fuzzy PID controller.

2.5. Error Fuzzy Controller

Figure 5 presents a block diagram of the error fuzzy controller. Error e_t and error variation Δe_t, which are derived from the speed feedback, are input variables of the error fuzzy controller. The output variable $u(t)$ is obtained when it is input into the error fuzzy controller. Figure 6 illustrates the seven-stage fuzzy membership function, in which two input variables, namely e_t and Δe_t, are divided into seven fuzzy sets: negative big (NB), negative medium (NM), negative small (NS), zero (ZE), positive small (PS), positive medium (PM), and positive big (PB) fuzzy sets. Table 5 details the rules for the seven-stage fuzzy controller. In the five-stage hysteresis controller, two input variables, namely, e_t and Δe_t, are divided into five fuzzy sets: NB, NS, ZE, PS, and PB. The rules for this controller are presented in Table 6.

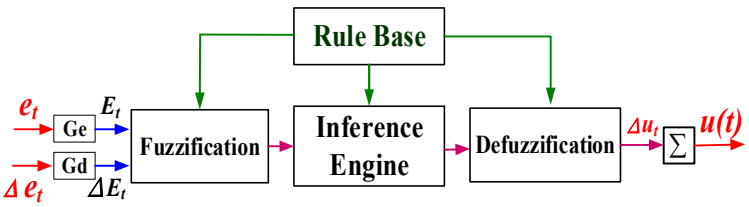

Figure 5. Block diagram of the error fuzzy controller.

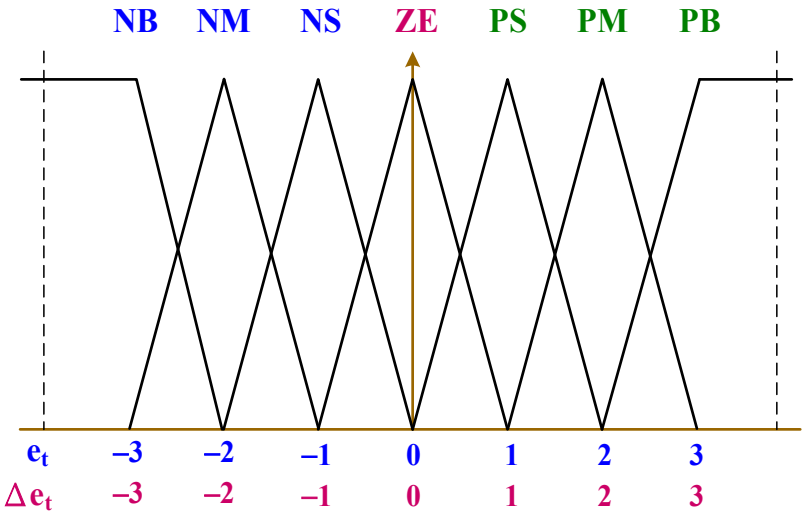

Figure 6. Seven–stage fuzzy membership function.

Table 5. Rules for the seven-stage fuzzy controller.

Δe_t \ e_t	PB	PM	PS	ZE	NS	NM	NB
PB	NB	NB	NM	NM	NS	NS	ZE
PM	NB	NM	NM	NS	NS	ZE	PS
PS	NB	NM	NS	NS	ZE	PS	PM
ZE	NM	NS	NS	ZE	PS	PS	PM
NS	NM	NS	ZE	PS	PS	PM	PB
NM	NS	ZE	PS	PS	PM	PM	PB
NB	ZE	PS	PS	PM	PM	PB	PB

Table 6. Rules for the five-stage fuzzy controller.

Δe_t \ e_t	PB	PS	ZE	NS	NB
PB	NB	NS	NS	ZE	ZE
PS	NB	NS	NS	ZE	PS
ZE	NS	NS	ZE	PS	PS
NS	NS	ZE	PS	PS	PB
NB	ZE	ZE	PS	PS	PB

2.6. MDMVV Switching Table

A major drawback of the traditional DTC hysteresis controller is the instability caused by the large torque and flux ripples generated by it. A five- or seven-stage hysteresis controller can be used to reduce the torque error for speed response or flux error, respectively. The torque error must be managed by using a fuzzy PID controller because this error requires a long processing time. Moreover, the torque error in a five-stage hysteresis controller has a synchronous action to the flux error in a seven-stage hysteresis controller. To solve the aforementioned problem, an MDMVV switching table is proposed. Figure 7 illustrates the torque error fuzzy controller with five-stage hysteresis control and the input variables of torque error (d_T, which is defined as $d_T = T_e^* - T_e$) and change rate of torque error (Δd_T). The output variable of this controller is the selected torque τ. The input variables of the five-stage hysteresis controller were divided into the PB, PS, ZE, NS, and NB fuzzy sets for torque error. The aforementioned sets were defined to be +2, +1, 0, −1, and −2, respectively. Figure 8 depicts the flux error fuzzy controller with seven-stage hysteresis control and the input variables of flux error (d_λ, which is defined as $d_\lambda = \lambda_e^* - \lambda_e$) and change rate of flux error (Δd_λ). The output variable of the aforementioned controller is the

selected flux. The input variables of the seven-stage hysteresis controller are divided into the PB, PM, PS, ZE, NS, NM, and NB fuzzy sets for flux error. These sets were defined to be +3, +2, +1, 0, −1, −2, and −3, respectively. After torque τ and flux φ had been computed, an MDMVV switching table was used to select an approximate output voltage set for four voltage vectors according to torque τ, flux φ, and sector S. Table 7 presents the MDMVV switching table.

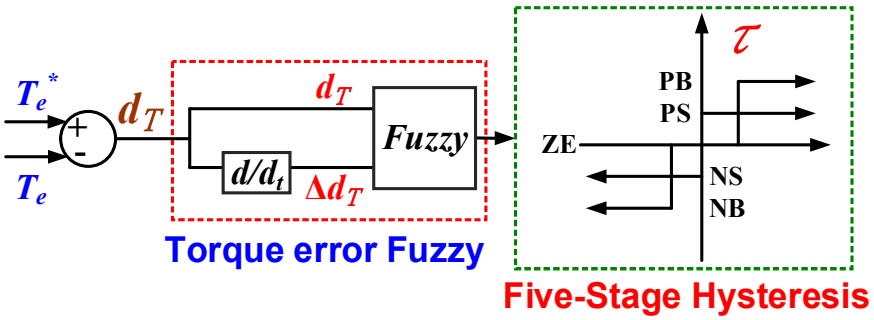

Figure 7. Torque error fuzzy controller with five-stage hysteresis control.

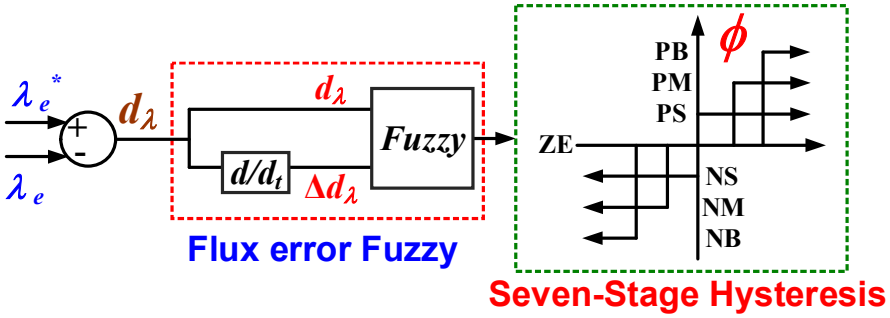

Figure 8. Flux error fuzzy controller with seven-stage hysteresis control.

If the MDMVV has a large positive flux (PB) and positive torque (PB) in sector S_1, the output voltage set was selected to be $V_2V_2V_2V_2$, which is denoted as 2222 in *Example (1)*. Each voltage (V_2) contributes an increment not only in torque, but also in flux. The total incremental value was +4 in *Example* (1). In *Example* (2) of Table 8, ZE was selected for the MDMVV because the flux remains unchanged, whereas NS was selected for the torque to reduce its value. The output voltage set for this example is $V_2V_7V_5V_0$, which increases the output toque (T_e) to near the recommend torque value (T^*_e). The other examples listed in Table 8 also describe the changing flux and torque. Figure 9 displays the time sequence of the MDMVV for the stator's torque. Four voltage vectors were employed in a sampling cycle T_S in this study, whereas only an output voltage vector is used in a traditional DTC sampling cycle. Thus, the proposed scheme is suitable for a heavy load or fluctuating torque and flux. Figure 10 illustrates variation d_T in response to sampling time T_s, which was equal to four times clock time T_C (i.e., $T_S = 4 \times T_C$ and $T_C = T_1 = T_2 = T_3 = T_4$). If current torque T_e was considerably lower than recommend torque T^*_e (NB) in sector S_1, voltage set $V_2V_2V_2V_2$ was selected to significantly increase the torque (PB), as detailed in *Example (1)* of Table 8. The status of current torque *Te* was PS, and an NS status was required to increase the torque to the recommend value for S_1 (T^*_e). According to Table 7, the aforementioned condition could be achieved using voltage set $V_2V_7V_5V_0$, as illustrated in Figure 10. When this voltage set was used, T_e was close to T^*_e.

Table 7. MDMVV switching table.

φ	τ	S1	S2	S3	S4	S5	S6
PB	PB	$V_2V_2V_2V_2$	3333	4444	5555	6666	1111
	PS	$V_2V_2V_2V_6$	3331	4442	5553	6664	1115
	ZE	$V_2V_2V_6V_6$	3311	4422	5533	6644	1155
	NS	$V_2V_6V_6V_6$	3111	4222	5333	6444	1555
	NB	$V_6V_6V_6V_6$	1111	2222	3333	4444	5555
PM	PB	$V_2V_2V_2V_2$	3333	4444	5555	6666	1111
	PS	$V_2V_2V_2V_7$	3330	4447	5550	6667	1110
	ZE	$V_2V_2V_6V_7$	3310	4427	5530	6647	1150
	NS	$V_2V_6V_6V_7$	3110	4227	5330	6447	1550
	NB	$V_6V_6V_6V_7$	1110	2227	3330	4447	5550
PS	PB	$V_2V_2V_2V_3$	3334	4445	5556	6661	1112
	PS	$V_2V_2V_2V_5$	3336	4441	5552	6663	1114
	ZE	$V_2V_6V_7V_7$	3300	4477	5500	6677	1100
	NS	$V_6V_6V_6V_3$	1114	2225	3336	4441	5552
	NB	$V_6V_6V_6V_5$	1116	2221	3332	4443	5554
ZE	PB	$V_2V_2V_3V_3$	3344	4455	5566	6611	1122
	PS	$V_2V_7V_3V_7$	3040	4757	5060	6717	1020
	ZE	$V_2V_3V_5V_6$	3461	4512	5623	6134	1245
	NS	$V_2V_7V_5V_0$	3067	4710	5027	6730	1047
	NB	$V_6V_5V_0V_0$	1677	2100	3277	4300	5477
NS	PB	$V_3V_3V_3V_2$	4443	5554	6665	1116	2221
	PS	$V_3V_3V_3V_6$	4441	5552	6663	1114	2225
	ZE	$V_3V_3V_0V_0$	4477	5500	6677	1100	2277
	NS	$V_5V_5V_5V_2$	6663	1114	2225	3336	4441
	NB	$V_5V_5V_5V_6$	6661	1112	2223	3334	4445
NM	PB	$V_3V_3V_3V_0$	4447	5550	6667	1110	2227
	PS	$V_5V_3V_3V_0$	6447	1550	2667	3110	4227
	ZE	$V_5V_5V_3V_0$	6647	1150	2267	3310	4427
	NS	$V_5V_5V_5V_0$	6667	1110	2227	3330	4447
	NB	$V_5V_5V_5V_5$	6666	1111	2222	3333	4444
NB	PB	$V_3V_3V_3V_3$	4444	5555	6666	1111	2222
	PS	$V_3V_3V_3V_5$	4446	5551	6662	1113	2224
	ZE	$V_3V_3V_5V_5$	4466	5511	6622	1133	2244
	NS	$V_5V_5V_5V_3$	6664	1115	2226	3331	4442
	NB	$V_5V_5V_5V_5$	6666	1111	2222	3333	4444

Table 8. Rules for the five-state fuzzy controller.

Example	*(1)*	*(2)*	*(3)*	*(4)*
Time	T_1,T_2,T_3,T_4	T_1,T_2,T_3,T_4	T_1,T_2,T_3,T_4	T_1,T_2,T_3,T_4
Vector	V_2,V_2,V_2,V_2	V_2,V_7,V_5,V_0	V_2,V_3,V_5,V_6	V_5,V_5,V_5,V_5
Torque	↑↑↑↑ (+4)	↑↓↓↓ (−2)	↑↑↓↓ (+0)	↓↓↓↓ (−4)
Flux	↑↑↑↑ (+4)	↑-↓- (+0)	↑↓↓↑ (+0)	↓↓↓↓ (−4)

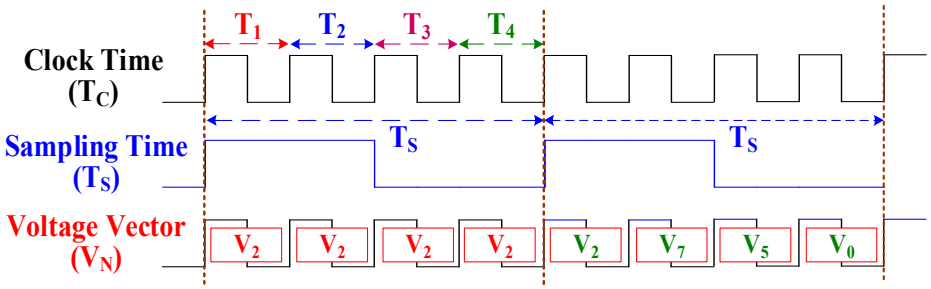

Figure 9. Time sequence of the MDMVV for the stator torque.

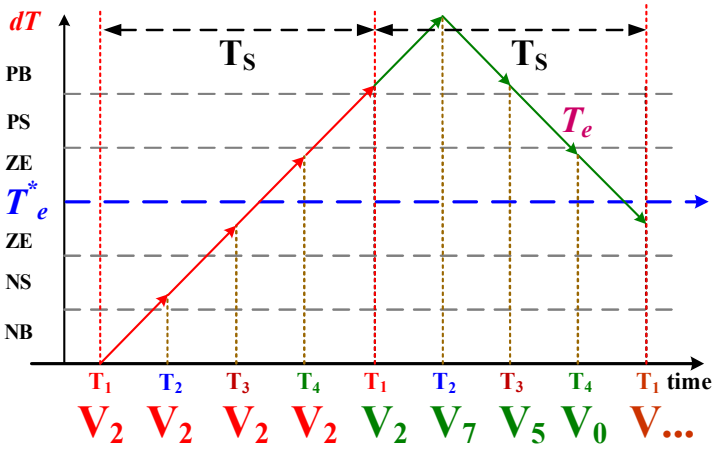

Figure 10. Variation in dT with sampling time (T_s), which is equal to four times clock time T_C.

2.7. Short Circuit Prevention

For a 0.75 hp IM, a dead time of 100 ns is essential for preventing short-circuit burning in the inverter of the IM control system. Figure 11 depicts the proposed short-circuit prevention scheme, which includes negative edge (Negedge) and positive edge (Posedge) control states, in the control signal [24]. In the Negedge state ($1 \rightarrow 0$), the "Up" signal changes from high (1) to low (0) when the control signal is turned off ($1 \rightarrow 0$). Moreover, the "Down" signal changes from low (0) to high (1) after the dead time (ΔT) is completed. In the Posedge state ($0 \rightarrow 1$), the "Down" signal changes from high (1) to low (0) when the control signal is turned on ($0 \rightarrow 1$). If the dead time (ΔT) is completed, the "Up" signal changes from low (0) to high (1). The proposed short-circuit prevention scheme is simple, and the dead time can be easily adjusted using the control signal.

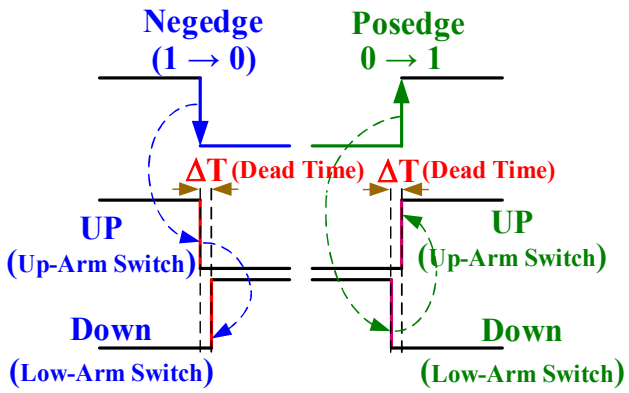

Figure 11. Proposed short-circuit prevention scheme.

3. Simulation and Measurement Results

A functional simulation was conducted using the Simulink package in MATLAB software (MathWorks, Natick, MA, USA). Figure 12 presents the functional simulation chart of the proposed MPDTC system for a three-phase IM drive. Input parameters Meas, Motor, and Ctrl were used to generate the voltage bus (V_bus). In the estimation module, the estimated flux (Flux_est) and estimated torque (Torque_est) were obtained, and used to generate the flux error (Flux_error) and torque error (Torque_error) by using the referenced flux (Flux_Ref) and referenced torque (Torque_Ref), respectively. A set of four voltage vectors were generated within a sampling time that comrpised four clock times, namely, T_1, T_2, T_3, and T_4, after passing through the fuzzy controller, fuzzy hysteresis, and MDMVV switching table.

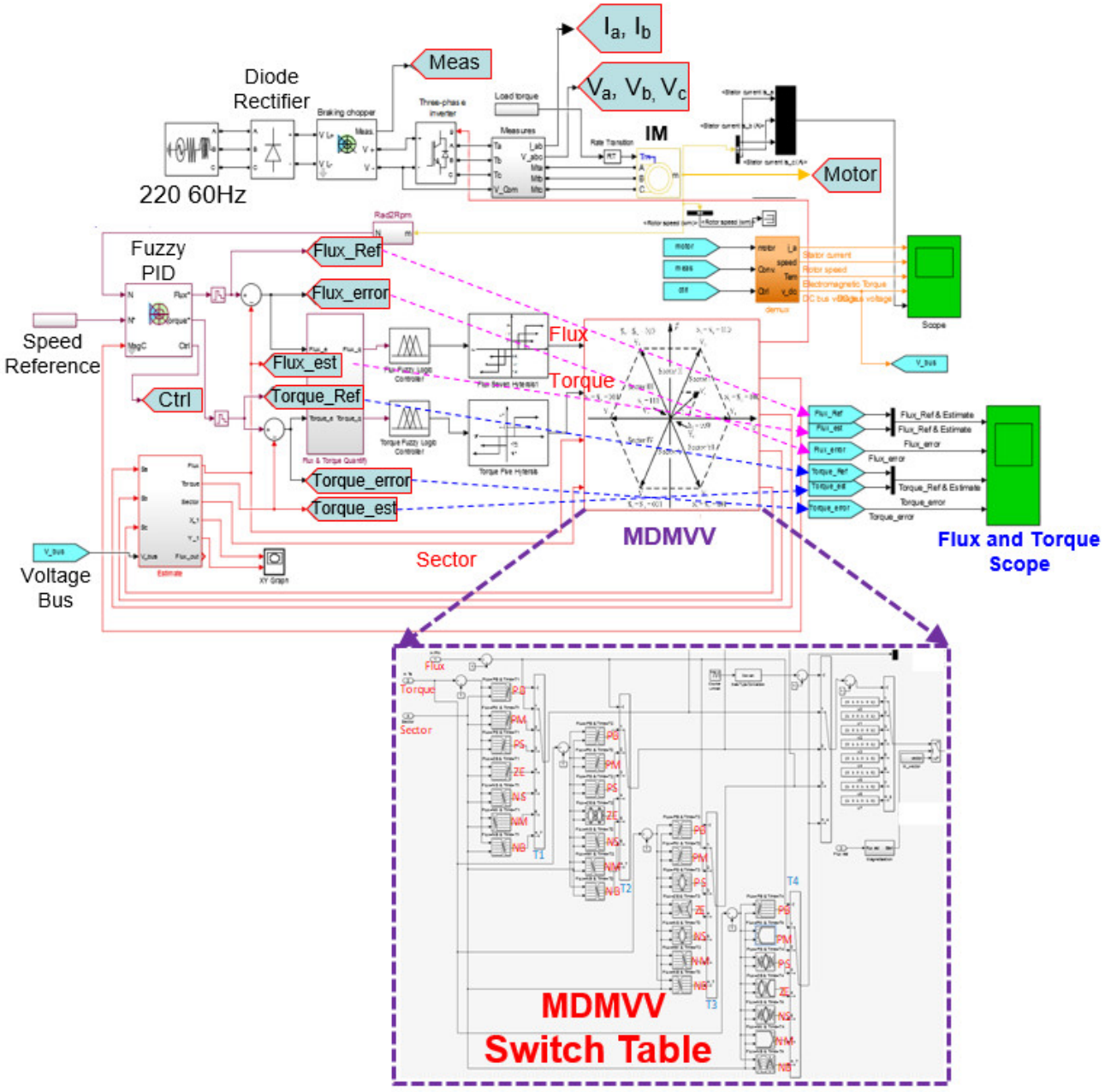

Figure 12. Functional simulation chart of the proposed MPDTC system for a three-phase IM drive.

According to the simulation results, the proposed MPDTC system exhibited smaller ripples in the stator's flux and torque than a conventional DTC system did with a hysteresis controller [23]. Figure 13 presents a comparison of the simulated flux errors of the proposed MPDTC and traditional DTC systems between 0 and 2 s, and Figure 14 presents a comparison of the two systems' simulated torque errors. The simulated flux and torque errors of the designed MPDTC system were smaller than those of conventional DTC system. The flux trajectories of the MPDTC and conventional DTC systems are depicted in Figure 15a,b, respectively. The aforementioned figure indicates that the proposed MPDTC system operated with a smaller flux border than the conventional DTC system does. The IM also operated smoothly with the proposed MPDTC system. Figure 16 illustrates the simulated line voltages in the U–V-phase, V–W-phase, and W–U-phase (V_{ab}, V_{bc}, and V_{ca}, respectively) for a three-phase IM drive.

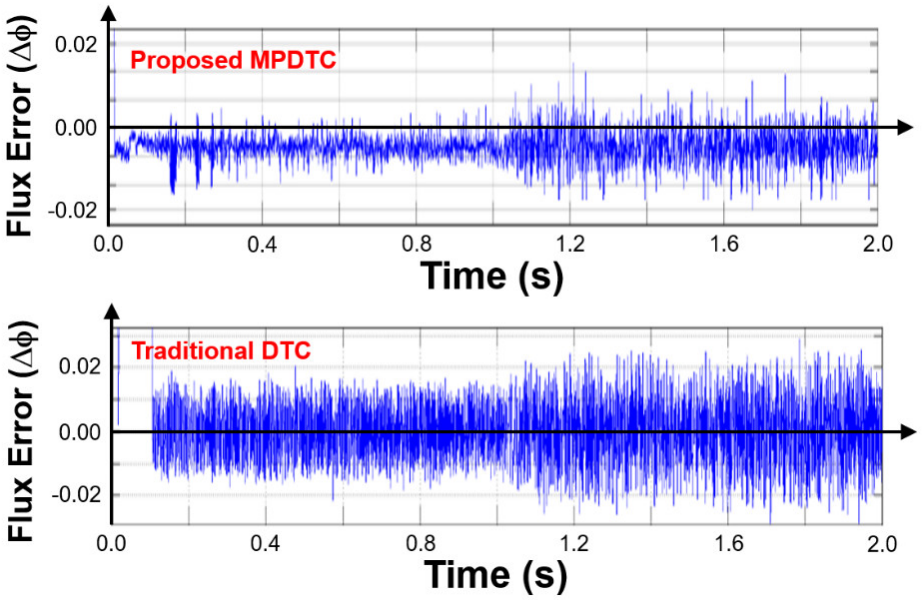

Figure 13. Simulated flux errors of the proposed MPDTC and traditional DTC systems between 0 and 2 s.

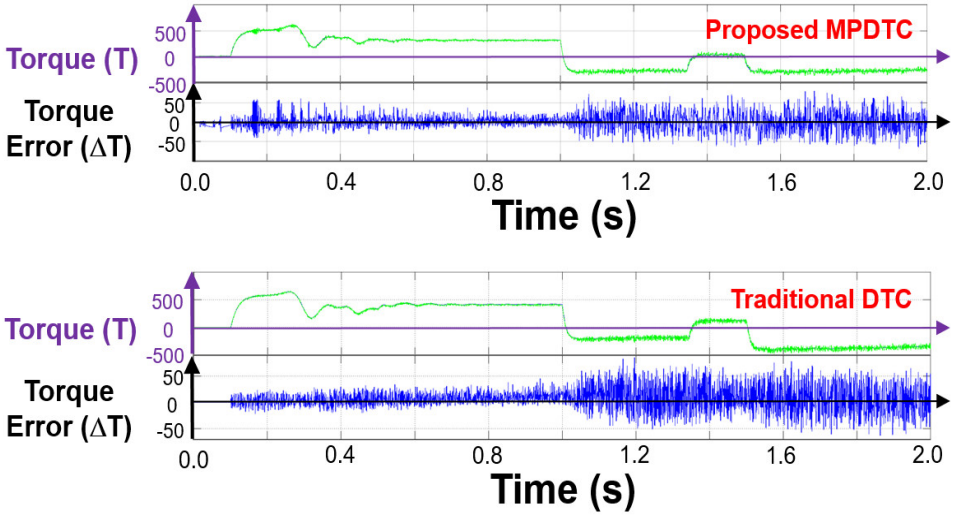

Figure 14. Simulated torque errors of the proposed MPDTC and traditional DTC systems between 0 and 2 s.

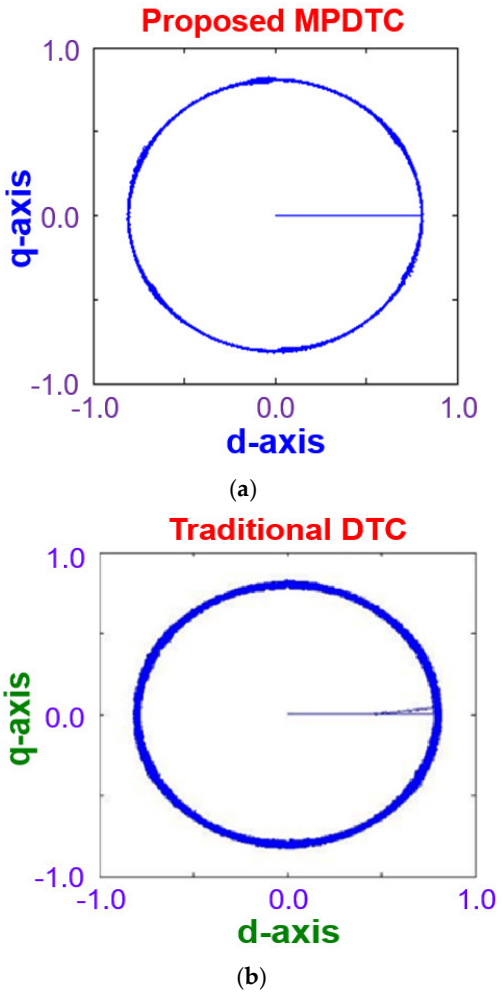

Figure 15. Simulated stator flux trajectory of (**a**) proposed MPDTC and (**b**) traditional DTC systems.

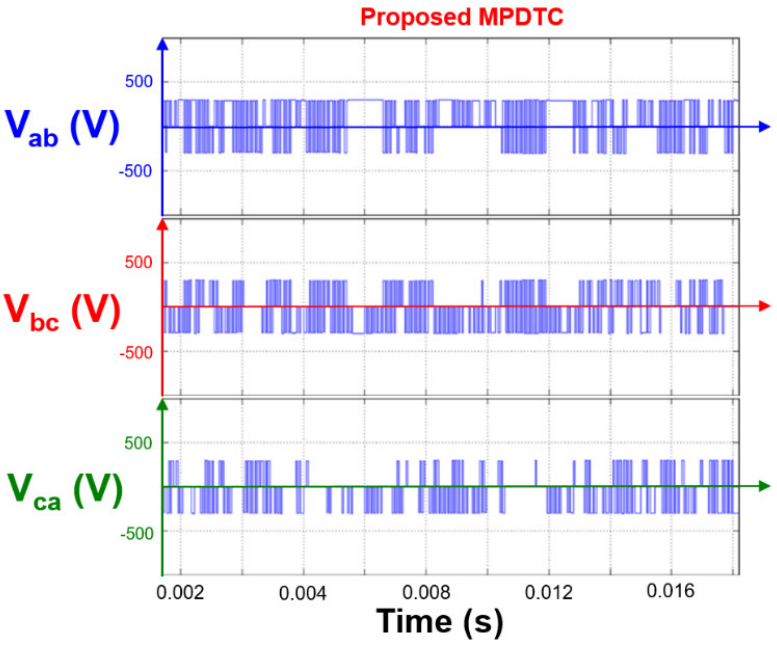

Figure 16. Simulated line voltages in U–V-, V–W-, and W–U-phases (V_{ab}, V_{bc}, and V_{ca}, respectively) for a three-phase IM drive.

After the functional simulations had been completed, the designed modules were implemented using the Verilog HDL. Figure 17 depicts the simulated voltage waveforms of six-arm signals in the inverter at a clock frequency of 10 MHz and a basic frequency of 1800 rpm (≈33.33 ms). The up-arm (US_i) and down-arm (DS_i) moved according to the inverse waveforms in each phase, with $i = a$, b, and c. Parameters US_a, US_b, and US_c represent the up-arm output voltages of the U-, V-, and W-phases, respectively. The behavioral simulation verified that the designed functions operate correctly within the ModelSim software.

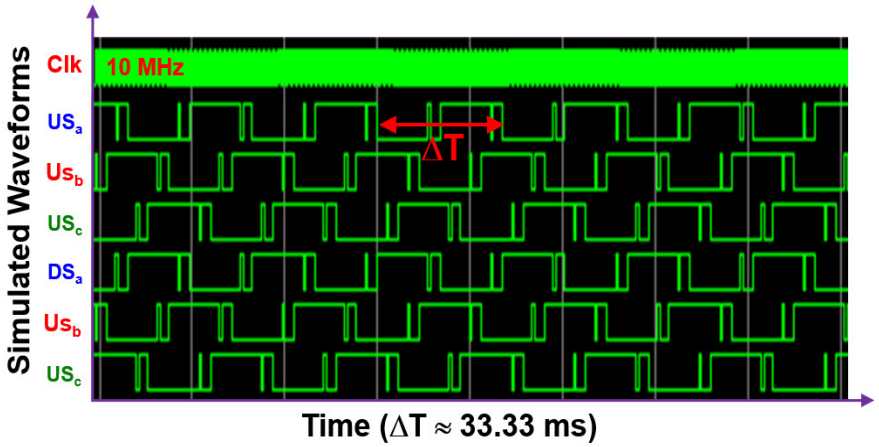

Figure 17. Simulated voltage waveforms of six-arm signals in the inverter at a clock frequency of 10 MHz and a basic frequency of 1800 rpm (≈33.33 ms).

Table 9 summarizes the system specifications of the proposed MPDTC ASIC. According to the simulation results, the proposed MPDTC had a test coverage of 95.64%, a fault coverage of 93.28%, and a power consumption of 2.457 mW at an operating frequency of 10 MHz and a supply voltage of 1.8 V. The gate count and chip area of this circuit (inclusive of the pads) were 99,188 and approximately 1.193 mm × 1.190 mm, respectively.

Table 9. System specifications of proposed MPDTC ASIC.

Items	Specifications
Technology	0.18-μm 1P6M CMOS
Supplied Voltage	1.8 V
Test Coverage	95.64%
Fault Coverage	93.28%
Operating Frequency	10 MHz
Sampling rate	100 kS/s
Power Consumption	2.457 mW
Gate Counts	99,188
Chip Size	1.193 mm × 1.190 mm
Pins	35

An FPGA development board was used to verify the designed functions, and a logic analyzer was used to analyze the measured digital signals. Figure 18 illustrates the measured waveforms of the six-arm voltage signals of the inverter. These waveforms were measured using the logic analyzer at a clock frequency of 10 MHz and a sampling frequency of 100 kHz. The generation of a dead time between the up-arm and the down-arm was essential for preventing the short-circuit burning of the three-phase IM. As illustrated in Figure 19, dead time of 100 ns that was measured in the W-phase with the logic analyzer was suitable for the adopted 0.75 hp IM.

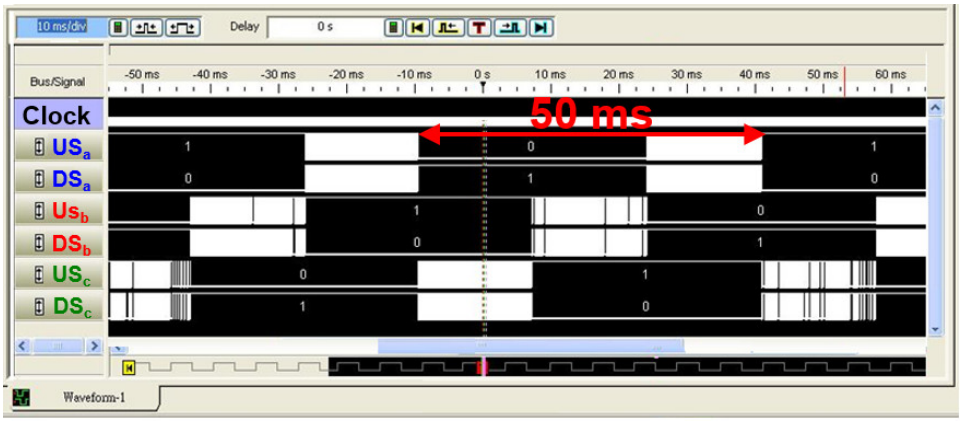

Figure 18. Behavioral simulation of waveforms of six–arm voltage signals of the inverter at a clock frequency of 10 MHz and a basic frequency of 1800 rpm (≈50 ms).

Figure 19. Dead time of 100 ns measured in the W-phase by using the logic analyzer.

Figure 20 depicts measured line currents I_{as} and I_{bs} at a sampling frequency of 100 kHz and a rotation frequency of 1200 rpm for a three-phase, 0.75-kW IM. As presented in (2), I_{as} and I_{bs} can be transformed into two-phase stator currents i^s_{ds} and i^s_{qs}, respectively, through trigonometric calculation. Figure 21 illustrates the measured up-arm voltages in the U-phase and V-phase (US_a and US_b, respectively). The proposed MPDTC ASIC and three-phase IM drive operated correctly, with the IM drive producing small ripples. Figure 22 presents a photomicrograph of the proposed MPDTC ASIC, which is fabricated by TSMC (Taiwan Semiconductor Manufacturing Company) and contains 35 pins.

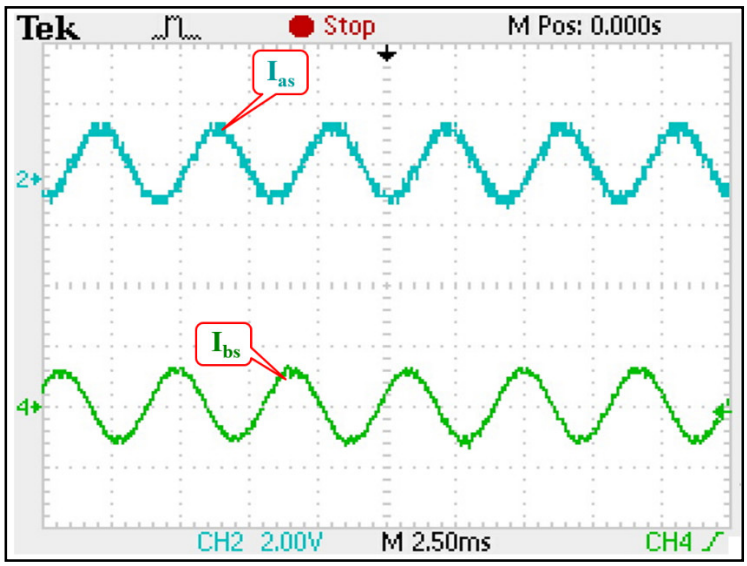

Figure 20. Measured line currents I_{as} and I_{bs} at a sampling frequency of 100 kHz and a rotation frequency of 1200 rpm for a three–phase IM.

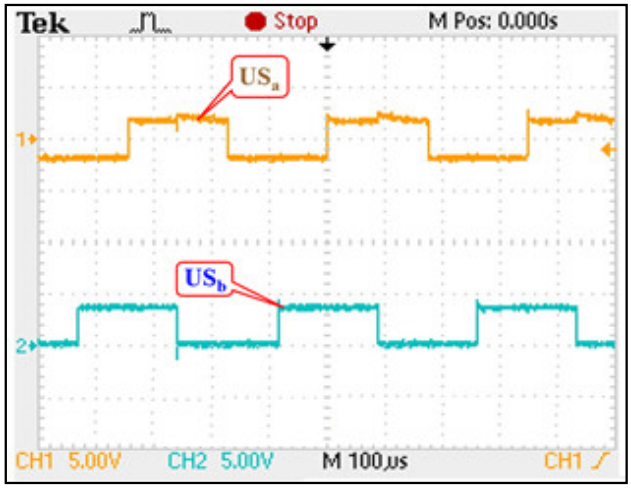

Figure 21. Measured up–arm voltages in the U–phase and V–phase (US_a and US_b, respectively).

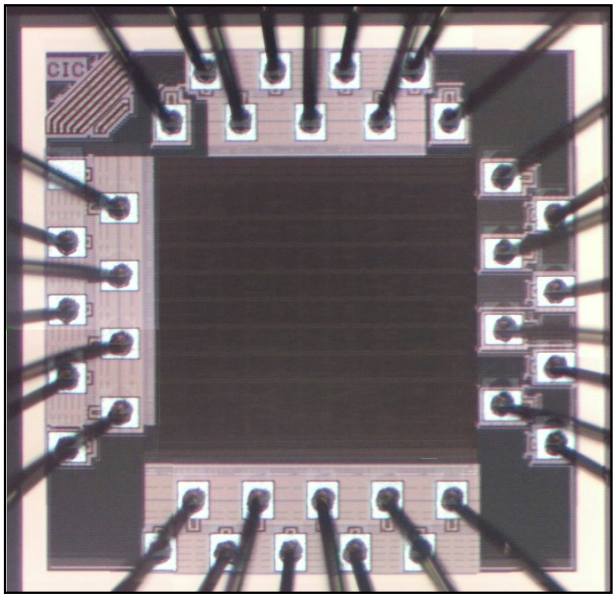

Figure 22. Photomicrograph of the proposed MPDTC ASIC.

4. Conclusions

In this study, an MPDTC ASIC with multistage hysteresis and fuzzy controller was proposed to enhance the stability and control of a 0.75-hp three-phase induction motor. ModelSim software was used to conduct functional simulation, and the Verilog HDL was employed to operate all modules of the proposed MPDTC system. After the designed functions had been verified using an FPGA development board, the proposed ASIC was fabricated using a TSMC 0.18 µm 1P6M CMOS process. Simulation results indicated that the stator flux trajectory of the proposed MPDTC ASIC was superior to that of a conventional DTC system with a hysteresis controller. In addition, the simulated torque and flux errors of the proposed MPDTC system were smaller than those of the conventional DTC system. The proposed fuzzy multistage hysteresis controller not only exhibited small torque and flux ripples, but also improved the performance of the IM drive by using four voltage vectors in a cycle. Measurement results revealed that the proposed ASIC had a dead time and power consumption of 100 ns and 2.457 mW, respectively, at an operating frequency of 10 MHz, a sampling rate of 100 kS/s, and a supply voltage of 1.8 V. Furthermore, the gate count and chip area of the proposed ASIC were 99,188 and approximately 1.193 mm × 1.190 mm, respectively. The objective of this study was to integrate the predictive DTC, fuzzy PID

controller, multistage hysteresis, and MDMVV switch table into an ASIC, and have small ripples by using four voltage vectors in a cycle. The proposed ASIC achieved good accuracy and robustness.

Author Contributions: Conceptualization, G.-M.S., L.-F.T., C.-C.H. and H.-Y.H.; methodology, L.-F.T. and H.-Y.H.; formal analysis, L.-F.T., C.-C.H. and H.-Y.H.; investigation, L.-F.T. and H.-Y.H.; writing—review and editing, G.-M.S., L.-F.T., C.-C.H. and H.-Y.H.; supervision, G.-M.S. and L.-F.T.; project administration, G.-M.S.; funding acquisition, G.-M.S. All authors have read and agreed to the published version of the manuscript.

Funding: This research was funded by the Ministry of Science and Technology (MOST), R.O.C., grant number MOST 110-2221-E-027-051 and by the NTUT-USTB Joint Research Program, grant number NTUT-USTB-110-01.

Acknowledgments: The authors thank the Ministry of Science and Technology (MOST), Taiwan, for its grant under the contract MOST 110-2221-E-027-051. The authors are also grateful to the Taiwan Semiconductor Research Institute (TSRI), Taiwan, for fabricating the test chip. This manuscript was edited by Wallace Academic Editing.

Conflicts of Interest: The authors declare no conflict of interest.

Appendix A

Table A1 shows all symbols used in Figure 1 to enhance the reader's understanding.

Table A1. All symbols used in the block diagram of the proposed MPDTC ASIC (Figure 1).

Symbol	Description	Symbol	Description
a	Upper arm voltage of A-phase	d_T	Torque error
$\overline{a}$	Lower arm voltage of A-phase	d_λ	Flux error
b	Upper arm voltage of B-phase	I_{as}	A-phase current of three-phase system
$\overline{b}$	Lower arm voltage of B-phase	I_{bs}	B-phase current of three-phase system
c	Upper arm voltage of C-phase	I_{ds}	D-phase current of two-phase system
$\overline{c}$	Lower arm voltage of C-phase	I_{qs}	Q-phase current of two-phase system
θ	Sector angle	P_a	Output waveform of channel A (Encoder)
φ	Magnetic flux	P_b	Output waveform of channel B (Encoder)
τ	Torque	S_a	UP-arm voltage of U-phase
λ	Flux	S_b	UP-arm voltage of V-phase
λ_{ds}	D-phase flux	S_c	UP-arm voltage of W-phase
λ_{qs}	Q-phase flux	T^*_e	Rated torque error
λ_e	Stator flux error	T_e	Torque error
λ_p	Predictive flux	T_p	Predictive torque
λ^*_s	Rated stator's flux	T_f	Torque error of fuzzy controller
λ_f	Flux error of fuzzy controller	V_{as}	A-phase voltage of three-phase system
ω_e	Speed error	V_{bs}	B-phase voltage of three-phase system
ω_p	Predictive speed	V_{cs}	C-phase voltage of three-phase system
ω_{ep}	Synthetic speed of speed error and predictive speed	V_{dc}	Dc voltage of the inverter
ω^*_r	Rated speed	V_{ds}	D-phase voltage of two-phase system
$\omega_{r(err)}$	Speed error	V_{qs}	Q-phase voltage of two-phase system
ω_r	speed feedback		

References

1. Takahashi, I.; Noguchi, T. A new quick-response and high-efficiency control strategy of an induction motor. *IEEE Trans. Ind. Appl.* **1986**, *5*, 820–827. [CrossRef]
2. Depenbrock, M. Direct self-control (DSC) of inverter-fed induction machine. *IEEE Trans. Power Electron.* **1988**, *3*, 420–429. [CrossRef]
3. Koratkar, P.J.; Sabnis, A. Comparative analysis of different control approaches of direct torque control induction motor drive. In Proceedings of the 2017 International Conference on Intelligent Computing, Instrumentation and Control Technologies (ICICICT), Kerala, India, 6–7 July 2017; pp. 831–835.
4. Mohamed, C.; Golea, A.; Benchouia, M.T. Implementation of a predictive DTC-SVM of an induction motor. In Proceedings of the 2015 4th International Conference on Electrical Engineering (ICEE), Boumerdes, Algeria, 13–15 December 2015; pp. 1–4.
5. Kumar, A.; Fernandes, B.G.; Chatterjee, K. Simplified SVPWM-DTC of 3-phase induction motor using the concept of imaginary switching times. In Proceedings of the 2004 30th Annual Conference of IEEE Industrial Electronics Society, Busan, Korea, 2–6 November 2004; pp. 341–346.
6. Baishan, M.; Haihua, L.; Jinping, Z. Study of fuzzy control in direct torque control system. In Proceedings of the 2009 International Conference on Artificial Intelligence and Computational Intelligence, Shanghai, China, 7–8 November 2009; pp. 129–132.
7. Geyer, T.; Papafotiou, G.; Morari, M. Model predictive direct torque control—Part I: Concept, algorithm and analysis. *IEEE Trans. Ind. Electron.* **2009**, *56*, 1894–1905. [CrossRef]
8. Papafotiou, G.; Kley, J.; Papadopoulos, K.G.; Bohren, P.; Morari, M. Model predictive direct torque control—Part II: Implementation and experimental evaluation. *IEEE Trans. Ind. Electron.* **2009**, *56*, 1906–1915. [CrossRef]
9. Benaicha, S.; Zidani, F.; Said, R.N.; Said, M.S.N. A novel direct torque fuzzy control of SVM-inverter-fed induction motor drive. In Proceedings of the 2013 4th International Conference on Power Engineering, Energy and Electrical Drives (POWERENG), Istanbul, Turkey, 13–17 May 2013; pp. 340–345.
10. Gomez-Espinosa, A.; Hernandez-Guzman, V.M.; Bandala-Sanchez, M.; Jimenez-Hernandez, H.; Rivas-Araiza, E.A.; Rodriguez-Resendiz, J.; Herrera-Ruiz, G. A new adaptive self-tuning fourier coefficients algorithm for periodic torque ripple minimization in permanent magnet synchronous motors (PMSM). *Sensors* **2013**, *13*, 3831–3847. [CrossRef] [PubMed]
11. Mendoza-Mondragon, F.; Hernandez-Guzman, V.M.; Rodriguez-Resendiz, J. Robust speed control of permanent magnet synchronous motors using two-degrees-of-freedom control. *IEEE Trans. Ind. Electron.* **2018**, *65*, 6099–6108. [CrossRef]
12. Chen, D.F.; Liao, C.W.; Yao, K.C. Direct torque control for a matrix converter based on induction motor drive systems. In Proceedings of the 2007 2nd International Conference on Innovative Computing, Information and Control (ICICIC), Kumamoto, Japan, 5–7 September 2007; pp. 1–4.
13. Zhang, J.; Li, L.; Zhang, L.; Dorrell, D.G. Hysteresis band current controller based field-oriented control for an induction motor driven by a direct matrix converter. In Proceedings of the 2017 43rd Annual Conference of the IEEE Industrial Electronics Society (IECON), Beijing, China, 29 October–1 November 2017; pp. 4633–4638.
14. Valenciaga, F.; Puleston, P.F.; Battaiotto, P.E. Variable structure system control design method based on a differential geometric approach: Application to a wind energy conversion subsystem. *IEEE Proc. Control. Theory Appl.* **2004**, *151*, 6–12. [CrossRef]
15. Hosseinzadeh, M.; Salmasi, F.R. Analysis and detection of a wind system failure in a micro-grid. *J. Renew. Sustain. Energy* **2016**, *8*, 43302–43315. [CrossRef]
16. Khalid, M.S.; Amin, M.R.; Hossain, M.M.; Anwer, M. Numerical round-off error in cellular phone services billing system. In Proceedings of the 2007 10th International Conference on Computer and Information Technology, Dhaka, Bangladesh, 27–29 December 2007; pp. 1–5.
17. McInerney, I.; Kerrigan, E.C.; Constantinides, G.A. Modeling round-off error in the fast gradient method for predictive control. In Proceedings of the 2019 IEEE 58th Conference on Decision and Control (CDC), Nice, France, 11–13 December 2019; pp. 1–6.
18. Cruz-Miguel, E.E.; Garcia-Martinez, J.R.; Rodriguez-Resendiz, J.; Carrillo-Serrano, R.V. A new methodology for a retrofitted self-tuned controller with open-source FPGA. *Sensors* **2019**, *20*, 6155. [CrossRef] [PubMed]
19. Montalvo, V.; Estevez-Ben, A.A.; Rodriguez-Resendiz, J.; Macias-Bobadilla, G.; Mendiola-Santibanez, J.D.; Camarillo-Gomez, K.A. FPGA-based architecture for sensing power consumption on parabolic and trapezoidal motion profiles. *Electronics* **2020**, *9*, 1301. [CrossRef]
20. Sathikumar, S.; Vithayathil, J. Digital simulation of field oriented control of induction motor. *IEEE Trans. Ind. Electron.* **1984**, *2*, 141–148. [CrossRef]
21. Sung, G.M.; Lee, C.T.; Huang, C.C.; Hsieh, H.Y. Predictive direct torque control application-specific integrated circuit with a fuzzy proportional-integral-derivative controller and a new round-off algorithm. *IEEE Access* **2022**, *10*, 48141–48152. [CrossRef]
22. Abdul Wahab, H.F.; Sanusi, H. Simulink model of direct torque control of induction machine. *Am. J. Appl. Sci.* **2008**, *5*, 1083–1090.
23. Sung, G.M.; Wang, W.Y.; Huang, Y.C. Predictive direct torque control with discrete multiple vector voltages and fuzzy hysteresis. In Proceedings of the 2016 IEEE International Conference on Systems, Man and Cybernetics (SMC), Budapest, Hungary, 9–12 October 2016; pp. 707–711.
24. Sung, G.M.; Wang, W.Y.; Lin, W.S.; Yu, C.P. Predictive direct torque control application-specific integrated circuit of an induction motor drive with a fuzzy controller. *J. Low Power Electron. Appl.* **2017**, *7*, 15. [CrossRef]
25. Anto, E.K.; Asumadu, J.A.; Okyere, P.Y. PID-based P&O MPPT controller for offgrid solar PV systems using Ziegler-Nichols tuning method to step, ramp and impulse inputs. *J. Multidiscip. Eng. Sci. Stud.* **2016**, *2*, 669–680.